Bridging the Catalyst Reactivity Gap between Au and Cu for the Reverse Water-Gas Shift Reaction

Yan, Dengxin; Kristoffersen, Henrik H.; Castelli, Ivano E.; Rossmeisl, Jan

Published in:
Journal of Physical Chemistry C

Link to article, DOI:
10.1021/acs.jpcc.2c06504

Publication date:
2022

Document Version
Early version, also known as pre-print

Bridging the Catalyst Reactivity Gap Between Au and Cu for the Reverse Water Gas Shift Reaction

Dengxin Yan[a], Henrik H. Kristoffersen[a]*, Ivano E. Castelli[b], and Jan Rossmeisl[a]

[a] Department of Chemistry, University of Copenhagen, Copenhagen 2100, Denmark

[b] Department of Energy Conversion and Storage, Technical University of Denmark, DK-2800 Kgs. Lyngby, Denmark

*E-mail: hhk@chem.ku.dk

Abstract

The reverse water gas shift reaction (rWGSR) is highly relevant for CO_2 utilization in sustainable fuel and chemical production. Both Au and Cu are interesting for rWGSR catalysis, but it turns out that the reactivities of Au and Cu are very different. In this study, we consider alloys made from Au, Ag, Cu, Pt, and Pd to identify surfaces with reactivities for CO_2 dissociation in between Cu(111) and Au(111). Additionally, interesting alloy surfaces should have activation energies for CO_2 dissociation that are only a little higher than the endothermic reaction energy. We find that certain Cu based alloys with Ag and Au meet these criteria, whereas alloys containing Pt or Pd do not. The low additional cost in activation energy occurs when the transition state and final state configurations are made to look very similar due to the placement of the different metal elements in the surface. Finally, we construct a kinetic model that compares the rate of the rWGSR to the estimated rate of unwanted side reactions (i.e. methane formation or coking) on Ag-Cu alloy surfaces with varying composition and random placement of the Ag and Cu atoms. The thermodynamics favor methane formation over rWGSR, but the model suggests that Ag-Cu alloy surfaces are highly selective for the rWGSR.

TOC Graphic

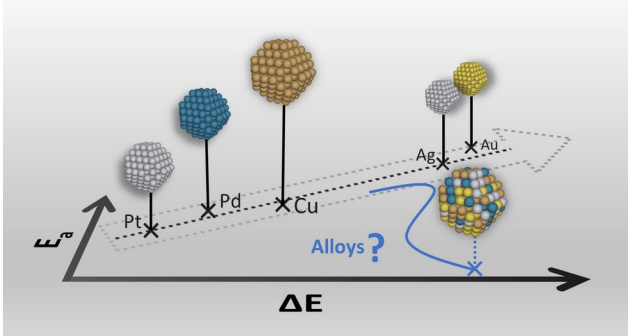

1. Introduction

CO_2 hydrogenation to CO via the reverse water gas shift reaction (rWGSR, eq 1) could be important for making the chemical industry more sustainable. The rWGSR is both a way to convert CO_2 into CO, which can be used directly as feedstock in syngas chemistry,[1] and a way to utilize hydrogen, which is the high energy chemical most straightforwardly produced by renewable powered electrochemistry.[2,3]

$$CO_2(g) + H_2(g) \rightarrow CO(g) + H_2O(g) \quad (1)$$

CO_2 hydrogenation can also form CH_3OH and CH_4 instead of CO.[4,5] Figure 1 shows reaction free energies to form the three products at the standard state pressure (i.e. 0.1 MPa pressure for all species) and with 2 MPa H_2 pressure. The thermodynamic data in Figure 1 is taken from ref [6–8]. Formation of the gas-phase CO is allowed at high temperatures, with Δ_rG for rWGSR being downhill above 1097 K at standard state pressure and above 629 K at 2 MPa H_2 pressure. On the other hand, CH_3OH is only stable ($\Delta_rG < 0$) at lower temperatures, i.e. below 267 K at standard state pressure and below 452 K with 2 MPa H_2 pressure. The formation of CO rather than CH_3OH can therefore largely be achieved by controlling the reaction conditions. More importantly, the equilibrium strongly favors CH_4 formation rather than CO formation below ~900 K or at increased H_2 pressure.[9,10] It is therefore important to have a catalyst that is selective towards CO instead of CH_4 when the goal is the rWGSR.

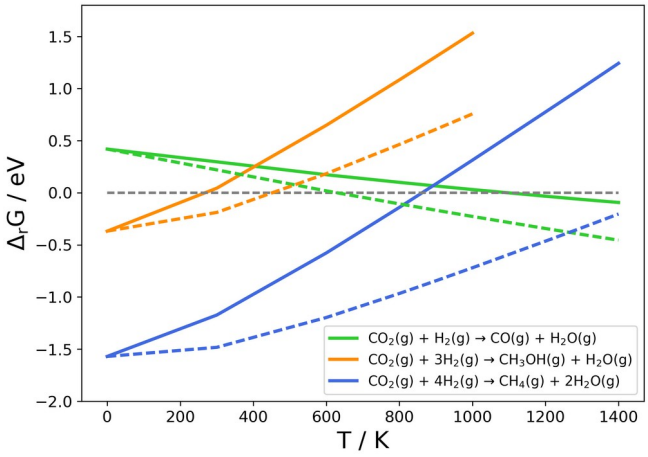

Figure 1: Reaction free energies[6–8] for CO_2 hydrogenation to CO (rWGRS), CH_3OH, and CH_4 at the standard state pressure (solid lines) and with 2 MPa H_2 pressure (dashed lines). The dashed lines are shifted from the solid lines by $\Delta n_{H2} \cdot k_B T \cdot \ln(20)$, where Δn_{H2} is the change in H_2(g) molecules in the reactions.

The main reaction step of interest is the initial CO_2 dissociation on the catalyst surface (reaction eq 2).

$$CO_2(g) + 2^* \rightarrow {}^*CO + O^* \quad (2)$$

In addition, two reaction steps concerning the fate of *CO are worth considering, namely the possible dissociation of *CO to *C and O* (reaction eq 3) and desorption of *CO to the gas phase (reaction eq 4).

$$^*CO + ^* \rightarrow C^* + O^* \quad (3)$$

$$^*CO \rightarrow CO(g) + ^* \quad (4)$$

Under normal rWGSR conditions the rate of CO_2 conversion to CO on transition metal catalysts is mainly controlled by the ability of the metal surface to catalyze reaction eq 2.[11–14] In Figure 2a, we have calculated reaction energy and activation energy for reaction eq 2 on pure transition metal (111) surfaces and Cu(100). The reactive (strong binding) Pt, Pd, and Cu have low reaction energy cost (ΔE)

and low activation energy (E_{TS}) compared to the inert (weak binding) Au and Ag metals. However, the selectivity towards the different CO_2 hydrogenation products is more strongly determined by the interaction between the metal surface and CO. Strong interaction could lead to C-O bond dissociation (reaction eq 3), which favors coking and CH_4 formation, whereas weak interaction favors CO desorption (reaction eq 4).[1] Metals are separable based on the energy cost for *CO desorption on one axis and the energy cost for *CO dissociation to C* and O* on the other, which we have calculated and plotted in Figure 2b. The inert Au(111), Ag(111), and to some extent Cu(111) favor *CO desorption and are expected to be more selective towards CO formation than the reactive Pd(111), Ni(111), Pt(111), Rh(111), and Ru(111) metals where C-O bond dissociation is not exceedingly costly. Indeed ref [15] found that Ag has lower rWGSR activity than Pd, Ni and Cu, but that Ag and Cu have higher selectivity towards CO than Pd and Ni. It was also recently shown that the Ni selectivity for the rWGSR can be increased by incorporating Zn. The presence of Zn weakens the CO adsorption energy on the Ni atoms, allowing for faster CO desorption.[16]

Experiments[17] have found that Cu(100) is better at facilitating CO_2 dissociation than Cu(111), which is also what we would expect from Figure 2a. However, Figure 2b suggests that Cu(100) also has a higher tendency to dissociate CO, which is unwanted, since the CO dissociation energy is much less costly on Cu(100) than on Cu(111).

With the thermodynamic and catalytic aspects in mind, experiments have obtained 50% or more conversion of CO_2 and >95% selectivity towards CO on both Au based (TiO_2-supported Au nanoparticles)[18] and Cu based (nanoceria-supported Cu nanoparticles)[19] catalysts at 673 K.[1] SiO_2-supported Pd-Fe nanoparticles are almost as good with 45% CO_2 conversion and 97% CO selectivity at 723 K,[20] but most other catalysts[1,21] either lack CO_2 conversion, CO selectivity, or utilize high temperatures where the equilibrium is shifted more towards CO formation.

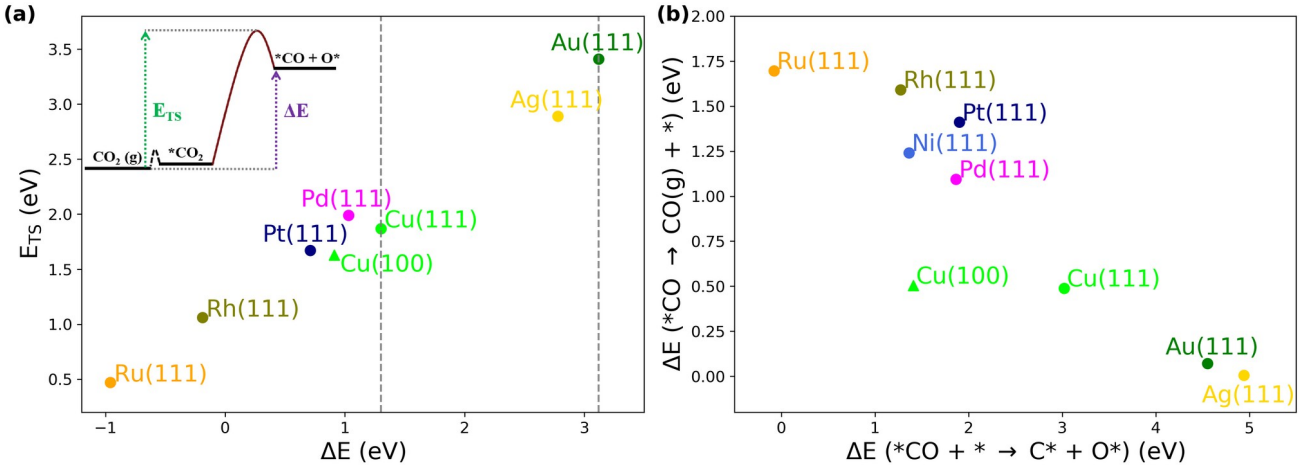

Figure 2: (a) Reaction energies (ΔE) and activation energies (E_{TS}) for CO_2(g) dissociation to *CO + O* on pure metal (111) surfaces and Cu(100). The ΔE and E_{TS} are explained by the insert. (b) Reaction energies for *CO + * → C* + O* versus reaction energies for *CO desorption on pure metal (111) surfaces and Cu(100). The dashed vertical lines show the large reactivity gap between Cu(111) and Au(111).

Cu[12–15,19] and Au[18,22–24] are both interesting for the rWGSR catalysis, so it is curious that there is such a large reactivity gap between these two metals. This is especially the case for reaction eq 2 on (111) surfaces (Figure 2a), where the reaction energy differs by 1.82 eV. Candidate catalysts with reactivities in this reactivity gap would likely be interesting for the rWGSR. According to our calculations, Ag(111) is slightly more reactive than Au(111), but there is no other pure metal in between Cu(111) and Au(111). One possibility is to use Au nanoparticles, which are expected to have increased reactivity compared to larger Au particles.[25] Actually, Au seems to be so inert that it works best as nanoparticles supported on oxide co-catalysts, where the oxide helps facilitate the CO_2 dissociation.[26,27] Unfortunately, nanoparticles often suffer more than larger particles from metal

oxidation, particle sintering and restructuring at high temperatures, which negatively affect their catalytic performance.[28–31]

Another possibility is to alloy two or more metals. Alloys are especially interesting because it might be possible to modify their activity and selectivity for rWGSR by changing their precise metal composition. Many bimetallic nanoparticles have recently been studied for the rWGSR, for instance, unsupported FeCo,[32] unsupported CuNi,[33] CuNi on Al_2O_3,[34] NiAu on SiO_2,[35] PtCo on TiO_2,[36] and CuIn on ZrO_2.[37]

In this study, we consider CO_2 dissociation (reaction eq 2) on (111) surfaces of alloys with up to four elements picked from Au, Ag, Cu, Pt, and Pd. We find multiple alloys with reactivities in between those of Au and Cu, indicating that the discrete reactivities of pure metals become a continuous reactivity distribution in the broad alloy composition space. This is not too surprising as it has already been shown that the adsorption energies of *CO and O* have broad distributions on multimetallic alloys.[38,39] However, we also find that the activation energy for CO_2 dissociation can be lowered in a very intuitive way by using an alloy surface that makes the transition state and final state look more similar. Alloys made from Ag, Cu, and Au are found to be most interesting for the rWGSR, as they span the reactivity gap between Cu and Au, have activation energies only slightly higher than the energy cost for CO_2 dissociation, and have low tendency to facilitate C-O bond dissociation. The low rate to facilitate C-O bond dissociation compared to the CO_2 to CO conversion rate on Ag-Cu alloy surfaces is confirmed by a kinetic model that considers both processes.

2. Methods

2.1 Computational details

We have performed density functional theory (DFT) calculations at the generalized gradient approximation (GGA) level with the Grid-based Projected Augmented Wave (GPAW) code.[40] The

RPBE functional[41] is used to describe exchange and correlation effects. The wave functions are expanded in plane waves with a 440 eV energy cutoff and the Brillouin zone is sampled with a Monkhorst-Pack grid of 2×2×1 k-points for surface slabs and Γ-point for gas-phase molecules.

We consider the reactivity of four types of FCC alloy slabs with the compositions A_3B, AB, A_2BC and ABCD, in addition to the pure metal slabs. The slabs have (4×4) surface cells exposing the (111) facet (Figure 3) and four atomic layer thicknesses. The A_3B, AB, A_2BC and ABCD bulk unit cells that the slabs are constructed from are shown in Supporting Information section S6. We use the Atomic Simulation Environment (ASE) package[42] to construct structural motifs such as cutting the alloy slabs from the bulk structures and adding adsorbates to the surfaces. We note that the B atoms in A_3B are sitting in a different surface pattern than the B/C atoms in A_2BC and the A/B/C/D atoms in ABCD (Figure 3). A consequence of this is that CO_2 can dissociate at four adjacent A atoms in A_3B, which is not possible on the AB, A_2BC, and ABCD surfaces.

We add 16 Å of vacuum in the z direction between the periodic images of the slabs. The atoms in the two bottom layers of the slabs are fixed in the bulk FCC positions, while the top two atomic layers are allowed to relax during geometry optimization. All the surfaces are optimized until the maximum force is lower than 0.03 eV/Å, while gas-phase molecules are relaxed to a maximum force of 0.01 eV/Å. The alloy lattice parameters are approximated as the composition weighted average of the DFT calculated lattice parameters for the pure metals (see Supporting Information section S6 for details).[43–45]

The computational details are similar to those used in as in ref [[46]], and the DFT energies can be directly compared. All structures and scripts for plots presented in this work are stored in a database, which can be found online at https://nano.ku.dk/english/research/theoretical-electrocatalysis/katladb/bridging-the-catalyst-reactivity-gap .

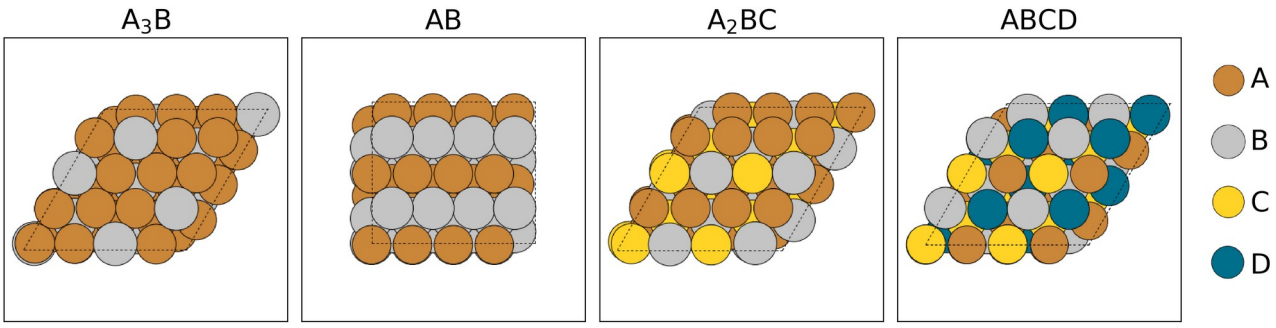

Figure 3: Illustration of (4×4) surface cells exposing the (111) facet for A_3B, AB, A_2BC and ABCD.

Figure 4 shows the DFT energy landscape for the rWGSR on Cu(111), Au(111) and AuCu. With our DFT parameters, the rWGSR has a DFT energy cost of 0.73 eV (independent of the surface), which is somewhat overestimated given the experimentally derived 0 K reaction enthalpy of ΔH^0_{0K} = 0.42 eV.[6] The DFT error in the rWGSR reaction energy is well-known and present in all the commonly used GGA functionals.[47]

We mainly focus on the $CO_2(g) \rightarrow *CO + O*$ part of rWGSR, for which, the reaction energy (ΔE) and activation energy (E_{TS}) are important. On Cu(111), we calculate ΔE and E_{TS} to be 1.30 eV and 1.87 eV (Figure 4a). With the PBE exchange-correlation functional instead of RPBE, the same values are 1.27 eV and 1.60 eV.[48] Consequently, we will predict slower CO_2 dissociation kinetics compared to studies using PBE, because we have a larger E_{TS} value. On Au(111), we calculate ΔE and E_{TS} to be 3.12 eV and 3.41 eV (Figure 4b). Again, our values are higher than the values calculated with PBE (2.86 eV and 3.16 eV).[48] Finally, we show the DFT energy landscape for rWGSR on AuCu, as an example of an alloy surface with ΔE between Cu(111) and Au(111) (Figure 4c). The ΔE and E_{TS} values are 2.13 eV and 2.30 eV on AuCu. We note that since CO_2 dissociation is uphill for the catalysts of interest, we have that $E_{TS} > \Delta E > 0$. A catalyst with a desirable ΔE, therefore always has E_{TS} at least as big as ΔE no matter how optimized the catalyst is.

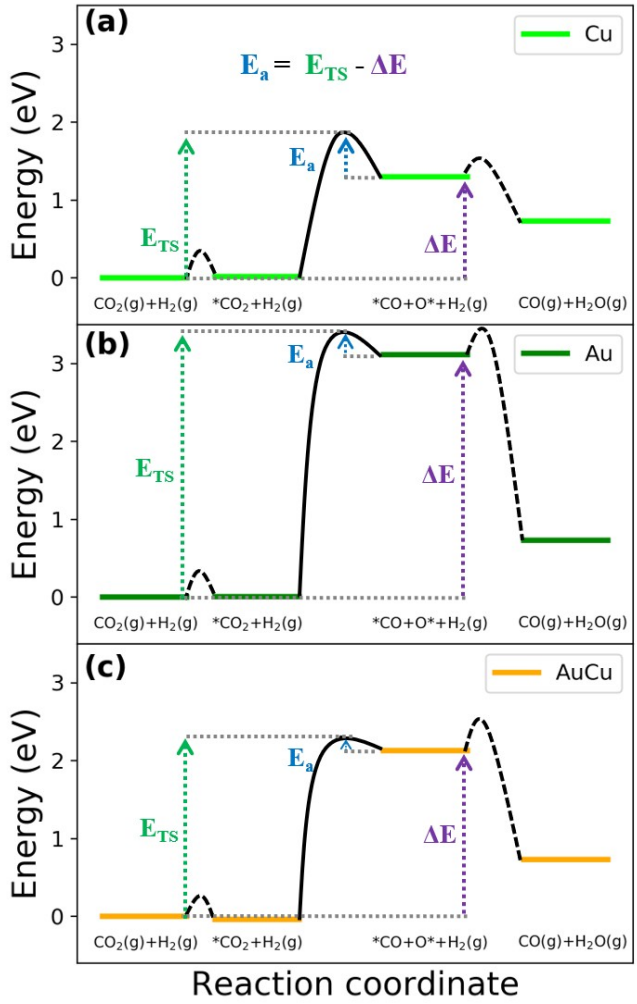

Figure 4: DFT energy diagram for rWGSR on (a) Cu(111), (b) Au(111) and (c) AuCu surfaces. E_{TS} is the energy of the transition state compared to the energy of the reactants (CO_2(g) and H_2(g)). ΔE is the reaction energy of the CO_2(g) → *CO + O* reaction step. Dashed lines indicate reaction barriers that we have not investigated in this study.

2.2 Computational methodology

Our first goal is to find alloy surfaces with ΔE in the reactivity gap between Au(111) and Cu(111). We therefore utilize a simple screening model developed for the water gas shift reaction, which uses

adsorption energies of O* and *CO on pure metal surfaces to estimate ΔE and E_{TS} for the possible alloy surfaces.[46] The alloys that are estimated to have ΔE in the reactivity gap and small $E_{TS} - \Delta E$ are further analyzed (see Supporting Information section S1 for details).

For each interesting alloy surface, we look for the most stable dissociated CO_2 configuration with the *CO and O* species at adjacent surface sites (*CO at an ontop site and O* at a hollow site). As an example, 24 configurations with co-adsorbed *CO and O* have been calculated on the $AuCu_2Pd(111)$ surface to find the most stable configuration (Figure S18 in the Supporting Information). The path from the initial state (IS) with CO_2 in the gas phase to the most stable dissociated final state (FS) will according to the Brønsted-Evans-Polanyi (BEP) relation,[49–52] often have the most stable transition state (TS) and therefore the lowest activation energy. The TS between molecular CO_2 and dissociated *CO and O* is obtained with the Climbing Image Nudged Elastic Band (CI-NEB) method.[53] In addition to the pathway to the most stable FS, we investigate pathways to other FS that are within ~0.02 eV of the most stable FS, if we suspect that their TS are more stable. We only present the pathway with the most stable TS.

We also use the insight presented in this study to obtain two pathways that have significantly less stable FS, but (in the case of Ag_3Cu) a more stable TS or (in the case $AgCu_3$) a TS within 0.05 eV of the most stable TS. These are denoted with the superscript “StableTS”.

Finally, we use the Ag_3Cu, AgCu, and $AgCu_3$ alloy surfaces to calculate E_{TS} for a range of possible Ag-Cu containing active sites and use these values in a kinetic model for Ag-Cu alloy surfaces with varying composition and random placement of the Ag and Cu atoms.

3. Results and discussion

3.1 Bridging the reactivity gap between Au and Cu.

Even though we have limited our study to five different elements and four types of (111) alloy surfaces, we find multiple surfaces with reactivities in between that of Au(111) and Cu(111). In Figure 5 we

mark the considered alloy surfaces with circles based on their ΔE and E_{TS} – ΔE values. We chose to plot E_{TS} – ΔE instead of E_{TS}, because the optimal value of E_{TS} – ΔE is 0, whereas the optimal value of E_{TS} is ΔE. The largest gap in ΔE between alloy (or pure) surfaces is reduced to 0.22 eV (between Ag_3Cu and $AgAuCu_2$), and interestingly, it is possible to change ΔE significantly without affecting E_{TS} – ΔE. This is especially true for alloys composed of Cu, Ag, and Au. For instance, AgCu, $AgAuCu_2$, AuCu, Ag_2AuCu, $AgAu_2Cu$, and Ag_3Au span 1.16 eV in ΔE but all have E_{TS} – ΔE of less than 0.2 eV. This is a substantial break from the linear scaling relation between ΔE and E_{TS} found for the CO_2 dissociation on pure metal surfaces.[54–56] Alloys containing Pt and Pd generally seem to be less optimized for the CO_2 dissociation and have E_{TS} – ΔE of at least 0.46 eV.

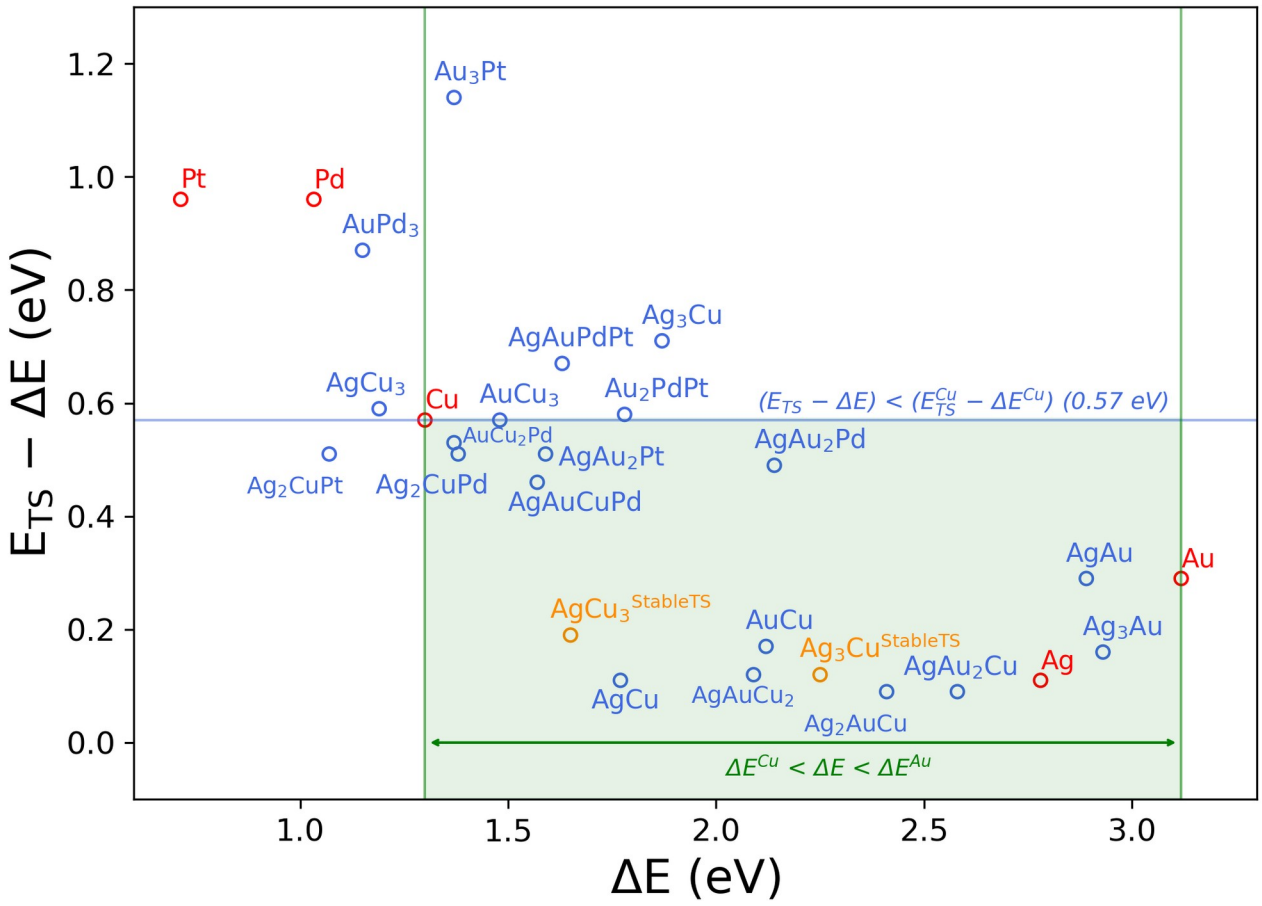

Figure 5: DFT reaction energies (ΔE) versus (E_{TS} – ΔE) DFT energies calculated for the CO_2(g) → *CO + O* reaction step on all the considered alloy surfaces. Blue circles show ΔE and (E_{TS} – ΔE) for the pathway to the stable FS on each alloy surface. Orange circles show ΔE and (E_{TS} – ΔE) for pathways where the TS is the most stable (in the case of $Ag_3Cu^{StableTS}$) or within 0.05 eV of the most stable TS (in the case of $AgCu_3^{StableTS}$), but where the FS is not the most stable.

We now take a closer look at the role of the four adjacent metal atoms involved in the CO_2 dissociation step to understand why many Cu, Ag, and Au containing alloy surfaces have small E_{TS} – ΔE over a large range of ΔE values. The CO_2 molecule dissociates through a TS where the O atom interacts with two metal atoms (designated B and C) and the CO interacts with one metal atom (designated D).[48,54,57] When CO_2 is fully dissociated the *CO is adsorbed at atom D, while the O* is adsorbed at atoms B, C and a third metal atom (designated A). The following discussion outlines how the metal atoms can be picked in a way to make TS and FS look more similar and thereby make E_{TS} – ΔE small.

We start with all four adjacent metal atoms being Ag, e.g. as found on the pure Ag(111) surface (Figure 6a). The Ag atoms are very inert and bind both *CO (on top) and O* (hollow) weakly. The energy to dissociate CO_2 is large (E_{TS} = 2.89 eV), but since there is barely any stabilization by binding the fragments to the Ag(111) surface, ΔE is almost as large as E_{TS}, and E_{TS} – ΔE becomes small (0.11 eV).

Next, we use the Ag_3Cu alloy surface to consider CO_2 dissociation at a site with three Ag atoms and one Cu atom (Figure 6b). When the Cu atom substitutes an Ag atom at position B or C, ΔE is lowered from 2.78 eV to 2.25 eV, while E_{TS} – ΔE remains low (0.12 eV). Cu binds O* significantly stronger than Ag, so at the TS where O* is sitting in a bridge configuration at positions B and C, the interaction between O* and Cu is optimized. The O* binds to an additional Ag atom at the FS, but that

does not provide strong stabilization. We note that the CO_2 dissociation site with three Ag atoms and one Cu atom has the most stable TS but not the most stable FS on the Ag_3Cu surface, i.e., it does not follow the BEP relation. We discuss the CO_2 dissociation pathway to the stable FS site on Ag_3Cu later.

We continue substituting Ag atoms with Cu atoms and get two Cu at positions B and C (Figure 6c). This site is the most stable *CO + O* adsorption site on the AgCu alloy surface. The second Cu atom lowers ΔE from 2.25 eV to 1.77 eV, but since the extra Cu atom stabilizes both ΔE and E_{TS}, the difference remains small ($E_{TS} - \Delta E = 0.11$ eV).

We substitute again to get three Cu atoms and one Ag atom (Figure 6d). Such a site is found on the $AgCu_3$ alloy surface. Having two Cu atoms at positions B and C and the third Cu atom at the *CO adsorption site (position D) lowers ΔE a little from 1.77 eV to 1.65 eV. However, not all of this stabilization is not present in E_{TS} giving a larger $E_{TS} - \Delta E$ (0.19 eV). The $AgCu_3$ alloy surface contains a CO_2 dissociation site with four Cu atoms and a more stable FS than the site with three Cu atoms and one Ag atom, however, the E_{TS} for the three Cu atoms and one Ag atom are within 0.05 eV of the most stable TS.

Substituting the last Ag for Cu to obtain a site with four Cu atoms (as on the Cu(111) surface) changes ΔE from 1.65 eV to 1.30 eV (Figure 6e). However, it barely changes the E_{TS} (from 1.84 eV to 1.87 eV) since the fourth Cu atom interacts very limited with the O* atom in the TS. The $E_{TS} - \Delta E$, therefore, increases to 0.57 eV. We generally find that the element at position A, which mostly binds the O* atom in the FS, influences the TS energy very little. Consequently, (111) alloy surfaces can be optimized for catalyzing the normal water gas-shift reaction by having reactive atoms at position B and C, and more inert atoms at position A.[46,57]

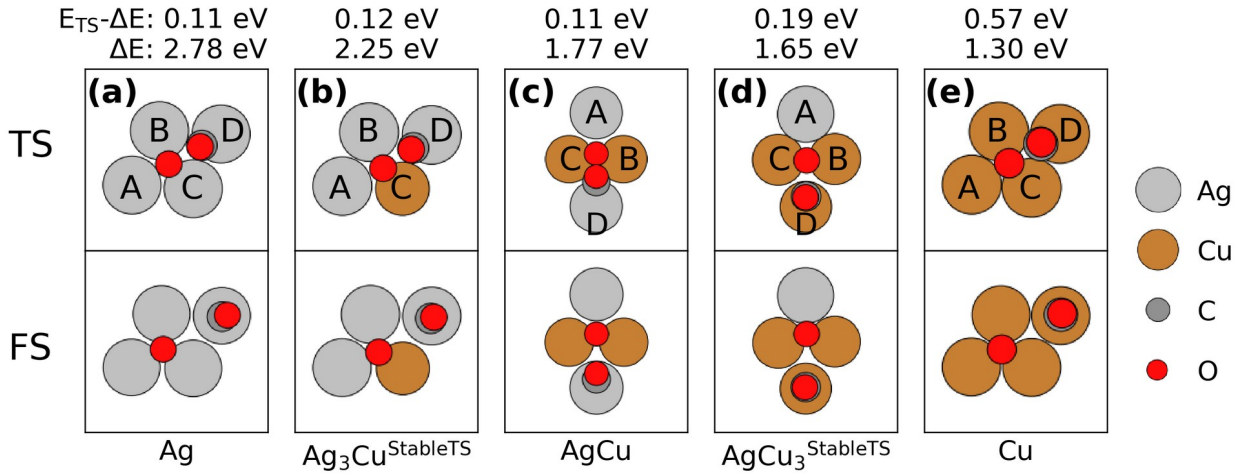

Figure 6: Illustration of TS and FS for CO_2 dissociation on (a) Ag, (b) $Ag_3Cu^{StableTS}$, (c) AgCu, (d) $AgCu_3^{StableTS}$, and (e) Cu. The FS shown for Ag, AgCu, and Cu are the stable FS on these alloy surfaces. The FS for $Ag_3Cu^{StableTS}$ and $AgCu_3^{StableTS}$ are not the most stable, since these surfaces have sites with one extra Cu atom, however the TS for $Ag_3Cu^{StableTS}$ is the most stable and the TS for $AgCu_3^{StableTS}$ is within 0.05 eV of the most stable TS found.

As mentioned earlier, the CO_2 dissociation site with three Ag atoms and one Cu atom (Figure 6b) does not have the most stable FS on the Ag_3Cu surface. Due to the makeup of the A_3B type surface cell (Figure 3), the Ag_3Cu surface also contains a CO_2 dissociation site, where the four adjacent metal atoms are two Cu and two Ag atoms, with the two Ag at positions B and C binding to O* in the TS state (Figure 7a). This adsorption site has a more stable FS than the CO_2 dissociation site with one Cu and three Ag atoms, but a less stable TS, since it is the Ag atoms and not the Cu atoms that binds to O* at the TS. This is an additional example that the scaling relation between ΔE and E_{TS} is subject to the precise makeup of the CO_2 dissociation site, but in this case, it is broken in to give a higher E_{TS}.

Figure 7b and Figure 7c illustrate what happens when Ag is exchanged for Au. In Figure 7b the *CO binding D position is changed from Ag to Au compared to Figure 6b. ΔE increases slightly from

2.25 eV to 2.41 eV, but the destabilization from Au is present both in the FS and the TS, so the (E_{TS} – ΔE) energy only changes from 0.12 eV to 0.09 eV. The situation is similar when a second Ag at position B is changed to Au (Figure 7c). ΔE increases from 2.41 eV to 2.58 eV, but E_{TS} – ΔE is unchanged.

Figure 7d and Figure 7e illustrate what happens when Ag is exchanged for Pt or Pd. Both Pt and Pd bind the CO molecule very strongly, so the most stable FS is obtained by having Pt or Pd at position D. The substitution of the Ag for Pt (or Pd) lowers ΔE from 2.25 eV to 1.07 eV (or 1.38 eV), however not all the stabilization is present at the TS so E_{TS} – ΔE increases from 0.12 eV to 0.51 eV.

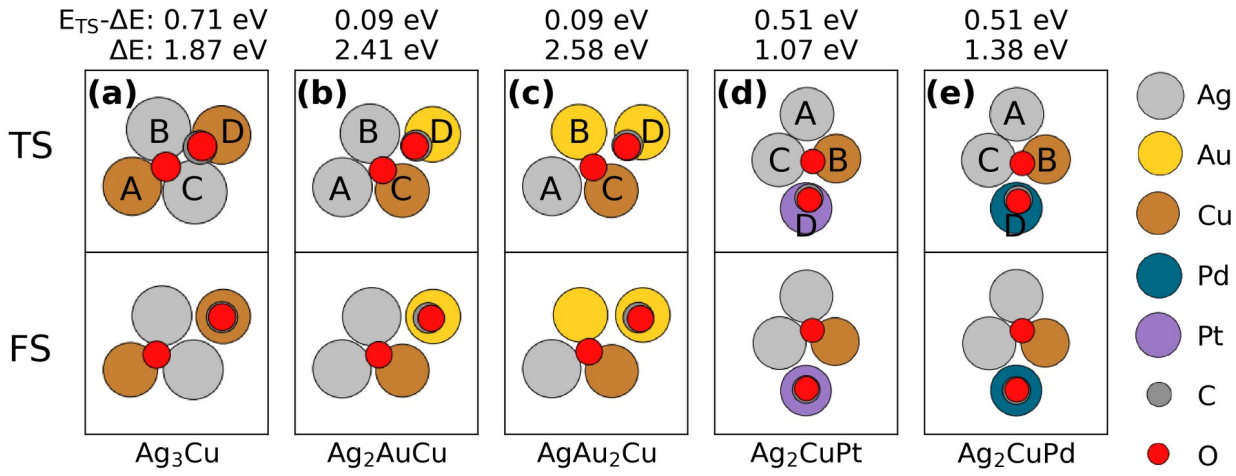

Figure 7: Illustration of TS and FS for CO_2 dissociation on (a) Ag_3Cu, (b) Ag_2AuCu, (c) $AgAu_2Cu$, (d) Ag_2CuPt, and (e) Ag_2CuPd. All the shown FS are the stable FS on these alloy surfaces.

It has been found that the reaction and activation energy for O_2 dissociation on multimetallic surfaces with random placement of the elements show scaling between the two sets of values, but with points being scattered around the optimum scaling line.[39] Our results for CO_2 dissociation indicate that the breaking of scaling relations can be understood by analyzing the makeup of the catalytic surface

sites. Consequently, the scaling relation is likely only a property that arises as the average behavior of all the possible surface site combinations.

3.2 Kinetic model for the rWGSR on Ag-Cu alloy surfaces.

The Ag-Cu alloy surfaces seem interesting for the rWGSR given that they can dissociate CO_2 with a range of reaction energies, have activation energies only slightly higher than the energy cost for CO_2 dissociation, and are made of elements with low tendencies to facilitate C-O bond dissociation. To validate these statements, we construct a kinetic model to obtain both the CO_2 dissociation rate and the CO dissociation rate on Ag-Cu alloy surfaces, hereby estimating both how active and selective the surfaces are for CO formation rather than methane formation or coking. The model includes CO_2 adsorption / desorption (eq 5), CO_2 dissociation / recombination (eq 6), CO desorption / adsorption (eq 7), and O* hydrogenation / dehydrogenation (eq 8). We follow the example for CO oxidation in [58] and assume that reactions eq 5, 7, and 8 are in quasi-equilibrium and that eq 6 is the rate determining step for the rWGSR. We ignore H* species and collect O* hydrogenation in (eq 8). It should be acceptable to neglect H* species, because the coverage of H* is low on Cu(111) and Ag-Cu alloys, and because the presence of H* doesn't seem to facilitate C-O bond breaking in CO_2 with lower barrier than the direct CO_2 dissociation to *CO and O* (see Supporting Information section S5 for details).[59] Finally, the kinetic model also includes *CO dissociation (eq 9), which we assume is irreversible and results in unwanted coking or methane formation.

$$CO_2(g) + * \rightleftharpoons *CO_2 \quad (5)$$

$$*CO_2 + * \rightleftharpoons *CO + O* \quad \text{(rate determining step)} \quad (6)$$

$$*CO \rightleftharpoons CO(g) + * \quad (7)$$

$$O* + H_2(g) \rightleftharpoons H_2O(g) + * \quad (8)$$

$$*CO + * \rightarrow C* + O* \quad \text{(irreversible)} \quad (9)$$

Most experiments are conducted at atmospheric pressure with high concentration of H_2 rather than high pressure of H_2.[1] We therefore assume that the rWGSR is carried out at 700 K and a total pressure of 0.1MPa, that the inlet gas mixture is 9:1 H_2 to CO_2, but that 40% of the CO_2 has been converted to CO and H_2O giving partial pressures of $p_{H2} = 0.86$, $p_{CO2} = 0.06$, $p_{CO} = p_{H2O} = 0.04$ (the equilibrium is $p_{H2} = 0.84$, $p_{CO2} = 0.04$, and $p_{CO} = p_{H2O} = 0.06$, as derived in the Supporting Information section S4).

We also need to decide the surface makeup of the Ag-Cu alloys. We note that the Ag-Cu phase diagram shows that at 700 K (and below) only bulk Ag with a small concentration of Cu and bulk Cu with a small concentration of Ag is thermodynamically stable.[60] However, several experimental groups have managed to synthesize Ag-Cu alloy nanoparticles with varied compositions and used these for catalysis.[61,62] An interesting limiting case is a solid solution, where the Ag and Cu atoms are randomly distributed in the surface with x_{Cu} and x_{Ag} molar fractions (where $x_{Ag} = 1-x_{Cu}$). The CO_2 dissociation rate is mainly determined by the four metal atoms at the dissociation site, so to describe an Ag-Cu solid solution we need to obtain ΔE and E_{TS} for all 16 combinations of Ag or Cu at the A, B, C, D sites. We have done this by conducting CI-NEB calculations for CO_2 dissociation at different positions on the Ag(111), Ag_3Cu, AgCu, $AgCu_3$, and Cu(111) surfaces and collected the results in Table 1. We ignore changes in entropy and zero-point energies (ZPE) between the IS and TS, but account for this in the backwards reaction by using ΔG instead of ΔE in the calculation of the backwards activation energy. Furthermore, we note that the experimental enthalpy for the full rWGSR is poorly reproduced with DFT and we estimate a DFT reaction energy error (ΔE_{error}) of 0.45 eV at 700 K (derived in the Supporting Information section S4). We also correct for this error in the backwards activation energy such that the activation energy for CO_2 recombination becomes $E_{TS} - (\Delta G - \Delta E_{error})$. This ensures that we get the correct overall thermodynamic for the rWGSR. We can now estimate the forward (k_6^+) and backward (k_6^-) rate constants for the reaction eq 6 at each A, B, C, D site using the formula from transition state theory (eq 10).[63]

$$k_6^+ = \frac{k_B T}{h} \cdot \exp\left(\frac{-E_{TS}}{k_B T}\right) \quad , \qquad k_6^- = \frac{k_B T}{h} \cdot \exp\left(\frac{-\left(E_{TS} - \left(\Delta G - \Delta E_{error}\right)\right)}{k_B T}\right) \tag{10}$$

The reaction rate for eq 6 (r_6, eq 11) further depends on the coverages of CO_2 (θ_{CO2}), *CO (θ_{CO}), and O* (θ_O), which due to the quasi-equilibrium also can be expressed by the equilibrium constants for reaction eq 5, 7, and 8 (K_5, K_7, and K_8, respectively), and the p_{H2}, p_{CO2}, p_{CO}, p_{H2O} partial pressures.

$$r_6 = k_6^+ \, \theta_{CO2} \, \theta_* - k_6^- \theta_{CO} \, \theta_O = k_6^+ \, K_5 \, p_{CO2} - k_6^- K_7^{-1} \, p_{CO} \, K_8^{-1} \, p_{H2O} \, p_{H2}^{-1} \tag{11}$$

We assume that *CO_2 has 0 eV DFT adsorption energy on all surfaces in the calculation of K_5, and use the adsorption energies for *CO and O* adsorbed at the 16 different A, B, C, D sites to calculate K_7 and K_8. The *CO is adsorbed at position D, the O* is adsorbed at positions A, B, C and we ignore co-adsorption interaction between the two species. Entropy, heating, and ZPE corrections are obtained from [6,64,65] and applied to all DFT reaction energies (see Supporting Information section S4 for details). The kinetic values for CO_2 dissociation at the 16 different A, B, C, D sites are collected in Table 1.

Table 1: CO_2 dissociation (eq 6) reaction rates (r_6) and backward and forward activation energies (E_{TS}, E_{TS} - (ΔG-ΔE_{error})), rate constants (k_6^+, k_6^-), and *CO (θ_{CO}) and O* (θ_O) coverages for every combination of the A, B, C, D sites. The properties are calculated on the specified alloy surfaces.

Alloy surface	A, B, C, D site	E_{TS} (eV)	k_6^+ (s^{-1})	E_{TS} - (ΔG-ΔE_{error}) (eV)	k_6^- (s^{-1})	θ_{CO}	θ_O	r_6 (s^{-1})
Ag(111)	Ag, Ag, Ag, Ag	2.89	2.27E-08	0.21	4.49E+11	1.08E-10	1.55E-17	4.68E-15
Ag_3Cu	Ag, Ag, Ag, Cu	2.67	8.72E-07	0.35	4.41E+10	3.64E-07	4.83E-18	1.31E-13
Ag_3Cu	Ag, Ag, Cu, Ag	2.37	1.26E-04	0.22	3.80E+11	1.08E-10	7.24E-14	2.71E-11
AgCu	Ag, Ag, Cu, Cu	2.09	1.31E-02	0.27	1.66E+11	1.35E-07	7.24E-14	1.50E-09
Ag_3Cu	Ag, Cu, Ag, Ag	2.37	1.26E-04	0.22	3.80E+11	1.08E-10	7.24E-14	2.71E-11
AgCu	Ag, Cu, Ag, Cu	2.09	1.31E-02	0.27	1.66E+11	1.35E-07	7.24E-14	1.50E-09
AgCu	Ag, Cu, Cu, Ag	1.88	4.25E-01	0.21	4.49E+11	4.08E-10	1.26E-10	7.85E-08
$AgCu_3$	Ag, Cu, Cu, Cu	1.84	8.25E-01	0.29	1.19E+11	3.10E-07	4.56E-12	2.86E-08

Ag_3Cu	Cu, Ag, Ag, Ag	2.8	1.01E-07	0.6	6.98E+08	1.08E-10	7.24E-14	1.87E-14
Ag_3Cu	Cu, Ag, Ag, Cu	2.58	3.88E-06	0.81	2.15E+07	3.64E-07	7.24E-14	3.60E-13
AgCu	Cu, Ag, Cu, Ag	2.2	2.11E-03	0.52	2.63E+09	4.08E-10	1.26E-10	3.69E-10
$AgCu_3$	Cu, Ag, Cu, Cu	2.29	4.75E-04	0.85	1.11E+07	3.10E-07	4.56E-12	9.78E-11
AgCu	Cu, Cu, Ag, Ag	2.2	2.11E-03	0.52	2.63E+09	4.08E-10	1.26E-10	3.69E-10
$AgCu_3$	Cu, Cu, Ag, Cu	2.29	4.75E-04	0.85	1.11E+07	3.10E-07	4.56E-12	9.78E-11
$AgCu_3$	Cu, Cu, Cu, Ag	2.12	7.95E-03	0.6	6.98E+08	1.51E-10	4.08E-09	1.47E-09
Cu(111)	Cu, Cu, Cu, Cu	1.87	5.02E-01	0.67	2.19E+08	3.10E-07	6.61E-10	7.50E-08

In the solid solution where the Cu and Ag atoms are randomly placed, each A, B, C, D site has a probability to occur given by the product of the molar fractions ($P_{A,B,C,D} = x_A\, x_B\, x_C\, x_D$). As an example, the A, B, C, D = Cu, Cu, Cu, Cu site has a probability of 1 on a pure Cu surface ($x_{Cu} = 1$) and a probability of 0.0625 on a surface with $x_{Cu} = 0.5$. The CO_2 dissociation rates on the Ag-Cu solid solution surfaces are then given by the rates of the different A, B, C, D sites weighted by their probability (eq 12).

$$r_{6,tot} = \sum x_A\, x_B\, x_C\, x_D \cdot r_2(x_A\, x_B\, x_C\, x_D) \tag{12}$$

In Figure 8 we plot the CO_2 dissociation rate as a function of the Cu molar fraction in the surface. The plot shows a strong improvement in activity by adding a small amount of Cu to pure Ag, followed by a more gradual additional improvement when going towards pure Cu. We also plot the smallest and highest activity of (A, B, C, D) sites with 3:1 Ag:Cu, 2:2 Ag:Cu and 1:3 Ag:Cu. At $x_{Cu} = 0.50$ the solid solution is a little less active than the (Ag, Cu, Cu, Ag) site and at $x_{Cu} = 0.75$ it is a little more active than the (Ag, Cu, Cu, Cu) site. However, interestingly, at $x_{Cu} = 0.25$ the solid solution is significantly more active than the (Ag, Ag, Cu, Ag) site. This highlights that in a solid solution with a small amount of Cu, there is still a small occurrence of sites with more Cu and higher activity (such as (Ag, Cu, Cu, Ag)) that due to the exponential nature of activity strongly improves the activity of the solid solution.

Overall, the CO_2 dissociation rates predicted by our kinetic model are very slow even for the pure Cu(111) surface. Some of this may be due to the high E_{TS} predicted by RPBE compared to PBE. However, it may also be that more reactive Cu facets are required for faster rates, for instance the Cu(100) surface[17] or even the steps[66] on Cu(100) surfaces. Although these facets are also likely to dissociate CO faster.

We can estimate the tendency of the Ag-Cu solid solution to dissociate *CO (eq 9) in much the same way as for $*CO_2$ dissociation, however, we must add two extra approximations. The first is that *CO dissociation is irreversible. This approximation is needed because we do not consider reactions with *C to give methane or coke and therefore do not know how fast the *C species are depleted. The second is to use the reaction energies ($\Delta E_{(*CO \rightarrow C^*+O^*)}$) for *CO dissociation instead of the activation energies. We do this because we have not performed CI-NEB calculations for *CO dissociation. Together these two approximations will give an upper limit for the *CO dissociation rate.

Both C* and O* adsorb in hollow sites on the surfaces, so six metal atoms (denoted A, B, C, D, E, F) are involved in the *CO dissociation reaction. However, we choose to divide the six metal atoms into two subgroups of three metal atoms by assuming that *CO adsorb at position D, that O* adsorb at positions A, B, C, that C* adsorb at positions D, E, F, and that O* and C* do not interact. With this separation $\Delta E_{(*CO \rightarrow C^*+O^*)}$ is then given by eq 13.

$$\Delta E_{(*CO \rightarrow C^*+O^*)}(A, B, C, D, E, F) = \Delta E_{O^*}(A, B, C) + \Delta E_{C^*}(D, E, F) - \Delta E_{*CO}(D) \quad (13)$$

There are 64 possible (A, B, C, D, E, F) combinations, but $\Delta E_{(*CO \rightarrow C^*+O^*)}$ is obtained from just four $\Delta E_{O^*}(A, B, C)$ values, four $\Delta E_{C^*}(D, E, F)$ values, and two $\Delta E_{*CO}(D)$ values. There is some ambiguity in which alloy surfaces we use to represent the different A, B, C, and D, E, F sites, but we choose to use the least stable adsorption energies for *CO and the most stable adsorption energies for O* and C* to again get an upper limit for the CO dissociation rates (see Supporting Information section S4 for details).

The CO dissociation rate on the Ag-Cu solid solution surfaces is also given by the rates of the different (A, B, C, D, E, F) sites weighted by their probability. In Figure 8 we plot the CO dissociation rate as a function of the Cu molar fraction in the surface. The CO dissociation rate is more than 5 orders of magnitude slower than the CO_2 dissociation rate, which strongly indicates that the Ag-Cu solid solution surfaces will be highly selective towards the rWGSR rather than methane formation or coking. However, the two rates have the same overall trends, highlighting that it is difficult to increase the rate for CO_2 dissociation without also getting more CO dissociation.

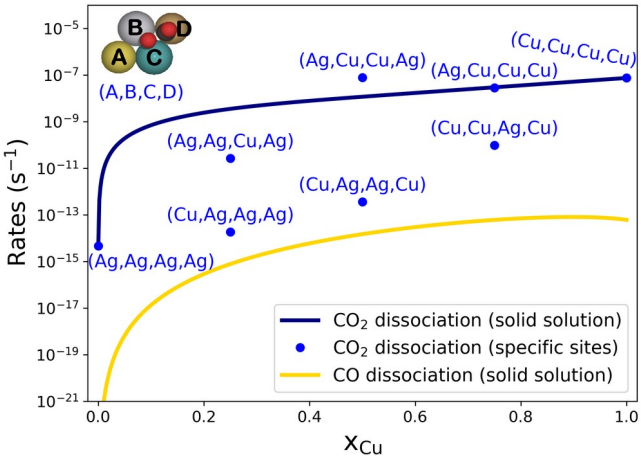

Figure 8: CO_2 and CO dissociation rates on Ag-Cu solid solution surfaces with varying composition and random placement of the Ag and Cu atoms. The plot also shows the activity of pure Ag(111) (labeled (Ag, Ag, Ag, Ag)) and pure Cu(111) (labeled (Cu, Cu, Cu, Cu)) and the smallest and highest activity from specific A, B, C, D sites with 3:1 Ag:Cu, 2:2 Ag:Cu, and 1:3 Ag:Cu composition. The reaction conditions modeled are 700 K and p_{H2} = 0.86, p_{CO2} = 0.06, p_{CO} = p_{H2O} = 0.04 partial pressures.

4. Conclusion

The Au(111) and Cu(111) reactivity for CO_2 dissociation differ by almost 2 eV even though both Au and Cu are used for rWGSR catalysis. We find that multimetallic (111) alloy surfaces made from Au,

Ag, Cu, Pt and Pd can largely fill the reactivity gap. Alloys consisting of Cu, Ag, and Au are most interesting because they both span more than 1 eV in reaction energies for CO_2 dissociation and have activation energies less than 0.2 eV larger than the reaction energies. This is a substantial break from the linear scaling relation between the two quantities found for CO_2 dissociation on pure metal surfaces. The similar activation and reaction energies can be understood at the atomic level because the catalytic sites with this property have metal atoms that stabilize both the transition state and final state. The Ag-Cu (111) alloy surfaces are further analyzed with a kinetic model, which shows that the surfaces are likely highly selective towards the rWGSR rather than methane formation or coking.

Acknowledgement

The authors acknowledge support from the Danish National Research Foundation Center for High-Entropy Alloy Catalysis (CHEAC) DNRF-149. D.Y. thanks for the support from the China Scholarship Council (CSC).

Supporting Information Available

Description of the simple screening model used to identify interesting alloys, identification of the most stable *CO + O* final state on each alloy surface, CI-NEB calculated potential energy surfaces for the CO_2 dissociation pathways, description of the kinetic model for reverse water gas shift and CO dissociation, discussion on why it's acceptable to neglect hydrogen adsorption, details regarding bulk alloy structures and lattice constants.

References

(1) Bahmanpour, A. M.; Signorile, M.; Kröcher, O. Recent Progress in Syngas Production via Catalytic CO_2 Hydrogenation Reaction. *Appl. Catal. B Environ.* **2021**, *295*, 120319.

(2) de Vasconcelos, B. R.; Lavoie, J. M. Recent Advances in Power-to-X Technology for the Production of Fuels and Chemicals. *Front. Chem.* **2019**, *7*, Article 392.

(3) Smolinka, T.; Ojong, E. T.; Garche, J. Chapter 8 - Hydrogen Production from Renewable Energies—Electrolyzer Technologies. In *Electrochemical energy storage for renewable sources and grid balancing*; Moseley, P. T., Garche, J., Eds.; Elsevier: Amsterdam, 2015; pp 103–128.

(4) Grabow, L. C.; Mavrikakis, M. Mechanism of Methanol Synthesis on Cu through CO_2 and CO Hydrogenation. *ACS Catal.* **2011**, *1*, 365–384.

(5) Wang, X.; Shi, H.; Szanyi, J. Controlling Selectivities in CO_2 Reduction through Mechanistic Understanding. *Nat. Commun.* **2017**, *8*, 513.

(6) *NIST-JANAF Thermochemical Tables*. https://janaf.nist.gov/.

(7) Goodwin, R. D. Methanol Thermodynamic Properties From 176 to 673 K at Pressures to 700 Bar. *J. Phys. Chem. Ref. Data* **1987**, *16*, 799–892.

(8) Wagman, D. D.; Evans, W. H.; Parker, V. B.; Schumm, R. H.; Halow, I.; Bailey, S. M.; Churney, K. L.; Nuttall, R. L. The NBS Tables of Chemical Thermodynamic Properties. Selected Values for Inorganic and C_1 and C_2 Organic Substances in SI Units. *J. Phys. Chem. Ref. Data* **1982**, *11*, Suppl. 2.

(9) González-Castaño, M.; Dorneanu, B.; Arellano-García, H. The Reverse Water Gas Shift Reaction: A Process Systems Engineering Perspective. *React. Chem. Eng.* **2021**, *6*, 954–976.

(10) Bown, R. M.; Joyce, M.; Zhang, Q.; Reina, T. R.; Duyar, M. S. Identifying Commercial Opportunities for the Reverse Water Gas Shift Reaction. *Energy Technol.* **2021**, *9*, 2100554.

(11) Nakamura, J.; Rodriguez, J. A.; Campbell, C. T. Does CO_2 dissociatively Adsorb on Cu Surfaces? *J. Phys. Condens. Matter* **1989**, *1*, SB149-SB160.

(12) Ernst, K.-H.; Campbell, C. T.; Moretti, G. Kinetics of the Reverse Water-Gas Shift Reaction over Cu(110). *J. Catal.* **1992**, *134*, 66–74.

(13) Ginés, M. J. L.; Marchi, A. J.; Apesteguía, C. R. Kinetic Study of the Reverse Water-Gas Shift Reaction over CuO/ZnO/Al_2O_3 Catalysts. *Appl. Catal. A Gen.* **1997**, *154*, 155–171.

(14) Fujita, S.-I.; Usui, M.; Takezawa, N. Mechanism of the Reverse Water Gas Shift Reaction over Cu/ZnO Catalyst. *J. Catal.* **1992**, *134*, 220–225.

(15) Choi, S.; Sang, B.-I.; Hong, J.; Yoon, K. J.; Son, J.-W.; Lee, J.-H.; Kim, B.-K.; Kim, H. Catalytic Behavior of Metal Catalysts in High-Temperature RWGS Reaction: In-Situ FT-IR Experiments and First-Principles Calculations. *Sci. Rep.* **2017**, *7*, 41207.

(16) Lin, S.; Wang, Q.; Li, M.; Hao, Z.; Pan, Y.; Han, X.; Chang, X.; Huang, S.; Li, Z.; Ma, X. Ni–Zn Dual Sites Switch the CO_2 Hydrogenation Selectivity via Tuning of the d-Band Center. *ACS Catal.* **2022**, *12*, 3346–3356.

(17) Eren, B.; Weatherup, R. S.; Liakakos, N.; Somorjai, G. A.; Salmeron, M. Dissociative Carbon Dioxide Adsorption and Morphological Changes on Cu(100) and Cu(111) at Ambient Pressures. *J. Am. Chem. Soc.* **2016**, *138*, 8207–8211.

(18) Kyriakou, V.; Vourros, A.; Garagounis, I.; Carabineiro, S. A. C.; Maldonado-Hódar, F. J.; Marnellos, G. E.; Konsolakis, M. Highly Active and Stable TiO_2-Supported Au Nanoparticles for CO_2 Reduction. *Catal. Commun.* **2017**, *98*, 52–56.

(19) Konsolakis, M.; Lykaki, M.; Stefa, S.; Carabineiro, S. A. C.; Varvoutis, G.; Papista, E.; Marnellos, G. E. CO_2 Hydrogenation over Nanoceria-Supported Transition Metal Catalysts: Role of Ceria Morphology (Nanorods versus Nanocubes) and Active Phase Nature (Co versus Cu). *Nanomaterials* **2019**, *9*, 1739.

(20) Park, J.-N.; McFarland, E. W. A Highly Dispersed Pd–Mg/SiO_2 Catalyst Active for Methanation of CO_2. *J. Catal.* **2009**, *266*, 92–97.

(21) Kattel, S.; Liu, P.; Chen, J. G. Tuning Selectivity of CO_2 Hydrogenation Reactions at the Metal/Oxide Interface. *J. Am. Chem. Soc.* **2017**, *139*, 9739–9754.

(22) Xu, H.; Li, Y.; Luo, X.; Xu, Z.; Ge, J. Monodispersed Gold Nanoparticles Supported on a Zirconium-Based Porous Metal–Organic Framework and Their High Catalytic Ability for the Reverse Water–Gas Shift Reaction. *Chem. Commun.* **2017**, *53*, 7953–7956.

(23) Ro, I.; Carrasquillo-Flores, R.; Dumesic, J. A.; Huber, G. W. Intrinsic Kinetics of Plasmon-Enhanced Reverse Water Gas Shift on Au and Au–Mo Interfacial Sites Supported on Silica. *Appl. Catal. A Gen.* **2016**, *521*, 182–189.

(24) Upadhye, A. A.; Ro, I.; Zeng, X.; Kim, H. J.; Tejedor, I.; Anderson, M. A.; Dumesic, J. A.; Huber, G. W. Plasmon-Enhanced Reverse Water Gas Shift Reaction over Oxide Supported Au Catalysts. *Catal. Sci. Technol.* **2015**, *5*, 2590–2601.

(25) Mavrikakis, M.; Stoltze, P.; Nørskov, J. K. Making Gold Less Noble. *Catal. Letters* **2000**, *64*, 101–106.

(26) Chen, Y.; Cheng, J.; Hu, P.; Wang, H. Examining the Redox and Formate Mechanisms for Water–Gas Shift Reaction on Au/CeO_2 Using Density Functional Theory. *Surf. Sci.* **2008**, *602*, 2828–2834.

(27) Bobadilla, L. F.; Santos, J. L.; Ivanova, S.; Odriozola, J. A.; Urakawa, A. Unravelling the Role of Oxygen Vacancies in the Mechanism of the Reverse Water–Gas Shift Reaction by Operando DRIFTS and Ultraviolet–Visible Spectroscopy. *ACS Catal.* **2018**, *8*, 7455–7467.

(28) Okonkwo, P. C.; Ige, O. O.; Barhoumi, E. M.; Uzoma, P. C.; Emori, W.; Benamor, A.; Abdullah, A. M. Platinum Degradation Mechanisms in Proton Exchange Membrane Fuel Cell (PEMFC) System: A Review. *Int. J. Hydrogen Energy* **2021**, *46*, 15850–15865.

(29) Popović, S.; Smiljanić, M.; Jovanovič, P.; Vavra, J.; Buonsanti, R.; Hodnik, N. Stability and Degradation Mechanisms of Copper-Based Catalysts for Electrochemical CO_2 Reduction. *Angew. Chemie Int. Ed.* **2020**, *59*, 14736–14746.

(30) Zhang, X.; Zhu, X.; Lin, L.; Yao, S.; Zhang, M.; Liu, X.; Wang, X.; Li, Y.-W.; Shi, C.; Ma, D. Highly Dispersed Copper over β-Mo_2C as an Efficient and Stable Catalyst for the Reverse Water Gas Shift (RWGS) Reaction. *ACS Catal.* **2017**, *7*, 912–918.

(31) Twigg, M. V; Spencer, M. S. Deactivation of Copper Metal Catalysts for Methanol Decomposition, Methanol Steam Reforming and Methanol Synthesis. *Top. Catal.* **2003**, *22*, 191–203.

(32) Calizzi, M.; Mutschler, R.; Patelli, N.; Migliori, A.; Zhao, K.; Pasquini, L.; Züttel, A. CO_2 Hydrogenation over Unsupported Fe-Co Nanoalloy Catalysts. *Nanomaterials* **2020**, *10*, 1360.

(33) Wang, L.-X.; Guan, E.; Wang, Z.; Wang, L.; Gong, Z.; Cui, Y.; Yang, Z.; Wang, C.; Zhang, J.; Meng, X.; Hu, P.; Gong, X.-Q.; Gates, B. C.; Xiao, F.-S. Dispersed Nickel Boosts Catalysis by Copper in CO_2 Hydrogenation. *ACS Catal.* **2020**, *10*, 9261–9270.

(34) Gioria, E.; Ingale, P.; Pohl, F.; Naumann d'Alnoncourt, R.; Thomas, A.; Rosowski, F. Boosting the Performance of Ni/Al_2O_3 for the Reverse Water Gas Shift Reaction through Formation of CuNi Nanoalloys. *Catal. Sci. Technol.* **2022**, *12*, 474–487.

(35) Zhang, X.; Han, S.; Zhu, B.; Zhang, G.; Li, X.; Gao, Y.; Wu, Z.; Yang, B.; Liu, Y.; Baaziz, W.; Ersen, O.; Gu, M.; Miller, J. T.; Liu, W. Reversible Loss of Core–Shell Structure for Ni–Au Bimetallic Nanoparticles during CO_2 Hydrogenation. *Nat. Catal.* **2020**, *3*, 411–417.

(36) Kattel, S.; Yu, W.; Yang, X.; Yan, B.; Huang, Y.; Wan, W.; Liu, P.; Chen, J. G. CO_2 Hydrogenation over Oxide-Supported PtCo Catalysts: The Role of the Oxide Support in Determining the Product Selectivity. *Angew. Chemie Int. Ed.* **2016**, *55*, 7968–7973.

(37) Li, M.; My Pham, T. H.; Ko, Y.; Zhao, K.; Zhong, L.; Luo, W.; Züttel, A. Support-Dependent Cu–In Bimetallic Catalysts for Tailoring the Activity of Reverse Water Gas Shift Reaction. *ACS Sustain. Chem. Eng.* **2022**, *10*, 1524–1535.

(38) Pedersen, J. K.; Batchelor, T. A. A.; Bagger, A.; Rossmeisl, J. High-Entropy Alloys as Catalysts for the CO_2 and CO Reduction Reactions. *ACS Catal.* **2020**, *10*, 2169–2176.

(39) Pedersen, J. K.; Batchelor, T. A. A.; Yan, D.; Skjegstad, L. E. J.; Rossmeisl, J. Surface Electrocatalysis on High-Entropy Alloys. *Curr. Opin. Electrochem.* **2021**, *26*, 100651.

(40) Enkovaara, J.; Rostgaard, C.; Mortensen, J. J.; Chen, J.; Dułak, M.; Ferrighi, L.; Gavnholt, J.; Glinsvad, C.; Haikola, V.; Hansen, H. A.; Kristoffersen, H. H.; Kuisma, M.; Larsen, A. H.; Lehtovaara, L.; Ljungberg, M.; Lopez-Acevedo, O.; Moses, P. G.; Ojanen, J.; Olsen, T.; Petzold, V.; Romero, N. A.; Stausholm-Møller, J.; Strange, M.; Tritsaris, G. A.; Vanin, M.; Walter, M.; Hammer, B.; Häkkinen, H.; Madsen, G. K. H.; Nieminen, R. M.; Nørskov, J. K.; Puska, M.; Rantala, T. T.; Schiøtz, J.; Thygesen, K. S.; Jacobsen, K. W. Electronic Structure Calculations

with GPAW: A Real-Space Implementation of the Projector Augmented-Wave Method. *J. Phys. Condens. Matter* **2010**, *22*, 253202.

(41) Hammer, B.; Hansen, L. B.; Nørskov, J. K. Improved Adsorption Energetics within Density-Functional Theory Using Revised Perdew-Burke-Ernzerhof Functionals. *Phys. Rev. B* **1999**, *59*, 7413–7421.

(42) Larsen, A.; Mortensen, J.; Blomqvist, J.; Castelli, I.; Christensen, R.; Dulak, M.; Friis, J.; Groves, M.; Hammer, B.; Hargus, C.; Hermes, E.; Jennings, P.; Jensen, P.; Kermode, J.; Kitchin, J.; Kolsbjerg, E.; Kubal, J.; Lysgaard, S.; Maronsson, J.; Maxson, T.; Olsen, T.; Pastewka, L.; Peterson, A.; Rostgaard, C.; Schiøtz, J.; Schütt, O.; Strange, M.; Thygesen, K.; Vegge, T.; Vilhelmsen, L.; Walter, M.; Zeng, Z.; Jacobsen, K. J. The Atomic Simulation Environment—a Python Library for Working with Atoms. *J. Phys. Condens. Matter* **2017**, *29*, 273002.

(43) Batchelor, T. A. A.; Pedersen, J. K.; Winther, S. H.; Castelli, I. E.; Jacobsen, K. W.; Rossmeisl, J. High-Entropy Alloys as a Discovery Platform for Electrocatalysis. *Joule* **2019**, *3*, 834–845.

(44) Vegard, L. Die Konstitution Der Mischkristalle Und Die Raumfüllung Der Atome. *Zeitschrift für Phys.* **1921**, *5*, 17–26.

(45) Denton, A. R.; Ashcroft, N. W. Vegard's Law. *Phys. Rev. A* **1991**, *43*, 3161–3164.

(46) Yan, D.; Kristoffersen, H. H.; Pedersen, J. K.; Rossmeisl, J. Rationally Tailoring Catalysts for the CO Oxidation Reaction by Using DFT Calculations. *ACS Catal.* **2022**, *12*, 116–125.

(47) Wellendorff, J.; Lundgaard, K. T.; Møgelhøj, A.; Petzold, V.; Landis, D. D.; Nørskov, J. K.; Bligaard, T.; Jacobsen, K. W. Density Functionals for Surface Science: Exchange-Correlation Model Development with Bayesian Error Estimation. *Phys. Rev. B* **2012**, *85*, 235149.

(48) Liu, X.; Sun, L.; Deng, W.-Q. Theoretical Investigation of CO_2 Adsorption and Dissociation on Low Index Surfaces of Transition Metals. *J. Phys. Chem. C* **2018**, *122*, 8306–8314.

(49) Evans, M. G.; Polanyi, M. Inertia and Driving Force of Chemical Reactions. *Trans. Faraday Soc.* **1938**, *34*, 11–24.

(50) Metiu, H.; Agarwal, V.; Kristoffersen, H. H. THE ROLE OF COMPUTATIONS IN CATALYSIS. In *Reviews in Computational Chemistry*; Parrill, A. L., Lipkowitz, K. B., Eds.; Wiley, 2018; Vol. 31, p 171.

(51) van Santen, R. A.; Neurock, M.; Shetty, S. G. Reactivity Theory of Transition-Metal Surfaces: A Brønsted−Evans−Polanyi Linear Activation Energy−Free-Energy Analysis. *Chem. Rev.* **2010**, *110*, 2005–2048.

(52) Wang, S.; Temel, B.; Shen, J.; Jones, G.; Grabow, L. C.; Studt, F.; Bligaard, T.; Abild-Pedersen, F.; Christensen, C. H.; Nørskov, J. K. Universal Brønsted-Evans-Polanyi Relations for C–C, C–O, C–N, N–O, N–N, and O–O Dissociation Reactions. *Catal. Letters* **2011**, *141*, 370–373.

(53) Henkelman, G.; Uberuaga, B. P.; Jónsson, H. A Climbing Image Nudged Elastic Band Method for Finding Saddle Points and Minimum Energy Paths. *J. Chem. Phys.* **2000**, *113*, 9901–9904.

(54) Gong, X.-Q.; Liu, Z.-P.; Raval, R.; Hu, P. A Systematic Study of CO Oxidation on Metals and Metal Oxides: Density Functional Theory Calculations. *J. Am. Chem. Soc.* **2004**, *126*, 8–9.

(55) Liu, Z.-P.; Hu, P. CO Oxidation and NO Reduction on Metal Surfaces: Density Functional Theory Investigations. *Top. Catal.* **2004**, *28*, 71–78.

(56) Jiang, T.; Mowbray, D. J.; Dobrin, S.; Falsig, H.; Hvolbæk, B.; Bligaard, T.; Nørskov, J. K. Trends in CO Oxidation Rates for Metal Nanoparticles and Close-Packed, Stepped, and Kinked Surfaces. *J. Phys. Chem. C* **2009**, *113*, 10548–10553.

(57) Wang, Z.; Hu, P. Rational Catalyst Design for CO Oxidation: A Gradient-Based Optimization Strategy. *Catal. Sci. Technol.* **2021**, *11*, 2604–2615.

(58) Chorkendorff, I.; Niemantsverdriet, J. W. Kinetics. In *Concepts of Modern Catalysis and Kinetics*; Wiley-VCH Verlag GmbH & Co. KGaA, 2003; pp 23–78.

(59) Yang, Y.; White, M. G.; Liu, P. Theoretical Study of Methanol Synthesis from CO_2 Hydrogenation on Metal-Doped Cu(111) Surfaces. *J. Phys. Chem. C* **2012**, *116*, 248–256.

(60) Subramanian, P. R.; Perepezko, J. H. The Ag-Cu (Silver-Copper) System. *J. Phase Equilibria* **1993**, *14*, 62–75.

(61) Rout, L.; Kumar, A.; Dhaka, R. S.; Dash, P. Bimetallic Ag-Cu Alloy Nanoparticles as a Highly Active Catalyst for the Enamination of 1,3-Dicarbonyl Compounds. *RSC Adv.* **2016**, *6*, 49923–49940.

(62) Wang, S.; Shi, Y.; Hou, Y.; Shan, S.-L.; Wang, H.; Lu, J.-X. Electrocatalytic Asymmetric Reduction of Ethyl Benzoylformate on Bimetallic Ag–Cu Cathodes. *J. Appl. Electrochem.* **2020**, *50*, 973–978.

(63) Chorkendorff, I.; Niemantsverdriet, J. W. Reaction Rate Theory. In *Concepts of Modern Catalysis and Kinetics*; Wiley-VCH Verlag GmbH & Co. KGaA, 2003; pp 79–128.

(64) Peterson, A. A.; Abild-Pedersen, F.; Studt, F.; Rossmeisl, J.; Nørskov, J. K. How Copper Catalyzes the Electroreduction of Carbon Dioxide into Hydrocarbon Fuels. *Energy Environ. Sci.* **2010**, *3*, 1311–1315.

(65) Campbell, C. T.; Sellers, J. R. V. The Entropies of Adsorbed Molecules. *J. Am. Chem. Soc.* **2012**, *134*, 18109–18115.

(66) Hagman, B.; Posada-Borbón, A.; Schaefer, A.; Shipilin, M.; Zhang, C.; Merte, L. R.; Hellman, A.; Lundgren, E.; Grönbeck, H.; Gustafson, J. Steps Control the Dissociation of CO_2 on Cu(100). *J. Am. Chem. Soc.* **2018**, *140*, 12974–12979.